Wing-Tail Under Forced Harmonic Pitch

K. J. B. Tan* and H. Hesse†
University of Glasgow Singapore, Singapore 599493

P. C. Wang‡
Singapore Institute of Technology, Singapore 138683

A wing-tail tandem configuration undergoing forced harmonic pitch is numerically simulated using Detached-Eddy Simulation (DES) coupled with an overset grid. This subjects a tail to a wing wake induced through forced pitch oscillations ($Re = 2.14 \times 10^4$, $k = 0.1$). The study therefore captures a flow separated wake with characteristic Leading and Trailing Edge Vortices (LEV/TEVs) emanated from the wing at the higher angles-of-attack in the harmonic pitch cycles. These vortices convect downstream to interact with the tail, which are shown to be significant to its loads. Assessing the tandem system individually shows that their lift dynamics can be empirically approximated using the Theodorsen's function, but limited by stall characteristics and variances in tail lift from the wing wake encounter. This leads to a direct correlation in wing-tail dynamics where the tail lift response can be distinguished into two components; the combination of its pitch-heave by the tail moment arm, and as a periodic gust based on the separated wing wake. The periodicity and phase lag of the wake encounter by the tail suggests that wake effects are accounted for with a gust component as a function of the convective tail length. The combination of these mechanisms synthesises the tails response from both forced harmonic motion and wing wake interaction, and is shown to be significant to the entire system. This contributes to insights on wake interactions in tandem configurations under dynamic conditions.

I. Nomenclature

α	=	angle-of-attack
α_0	=	nominal angle-of-attack
$C_{L,D,M}$	=	coefficient of lift, drag, pitch moment
$C(k)$	=	Theodorsen's function
Co	=	Courant number
C_p	=	pressure coefficient
C	=	chord
Δ_{wake}	=	wake block cell size
k	=	reduced frequency
M	=	Mach number
Re	=	Reynolds number
t_c	=	characteristic time-step
U	=	velocity magnitude
ν	=	kinematic viscosity
ω_z	=	span-wise vorticity component
y^+	=	dimensionless first-cell height

*Postgraduate Research Student, Aerospace Division, AIAA Student Member.
†Assistant Professor, Aerospace Division, AIAA Member.
‡Assistant Professor, Engineering Cluster.

II. Introduction

Wake phenomena are known to interact with secondary surfaces within the same flow field. This is critical, as flows over obstacles can produce wakes that convect downstream to become aerodynamically significant to other bodies in proximity. Fluctuating quantities from shear layer instabilities and vortex shedding coupled with a region of reduced dynamic pressure can alter fluid flow behaviour, such as diminished surface forces from local Reynolds number changes, and induced unsteadiness from fluctuating quantities. Wake effects on aerodynamics have to be considered in engineering design. An aerodynamic design that accounts for wake effects is the horizontal stabilizer of a conventional fixed wing aircraft. The horizontal stabilizer is the dominant contributor to stability, and therefore its assessment of its pitch authority against local airflow properties is crucial to desirable flight characteristics. As the tail lies downstream of the wings, the interference of airflow from the wing's wake alters its performance. To account for change in dynamic pressure, the resulting stabilizer effectiveness is often treated with an efficiency factor taken as a dynamic pressure ratio relative to the freestream [1]. In addition, the downward deflection of airflow from the wings as a result of lift also alters the stabilizers effective angle-of-attack. Accounting for these effects are challenging, considering that the wake properties are dynamic as a function of attitude and trim.

It is argued that wing wake effects are generally present and experienced by the tail throughout an aircraft flight regime [2]. In wing wake patterns relative to tails, the tail height can alleviate wing wake effects, such as a T-tail [3]. However, this risks deep-stall as pitch authority can be further reduced by the blanketing of the wing wake at higher angles-of-attack. It is arguable that a low-tail design under identical stalling conditions may avoid this predicament as the wake will then be shed over the stabilizer instead. Regardless of tail height, observations from low-speed stall [4] suggests that the vertical extent of the wake could still be adequately large enough to interact with even a low-tail design at stall. At higher angles-of-attack, the adverse effects of the wing wake on the tail become more dominant [4]. The wake width grows as the flow separates over the wing, resulting in a region of reduced dynamic pressure. This develops into what is larger than the characteristic length of the wing, blanketing the tail and reducing its pitch effectiveness.

As the wake width widens downstream, its characteristics become a function of tail length. According to Silverstein and Bullivant [5], an aircraft tail typically lies 0.75 wing semi-spans downstream [6, 7]. Suitable turbulence modelling techniques are required as the use of RANS methods may exhibit dissipative behaviours for wakes especially at these distances. This is reported by Breuer et al. [8] where the modelling of effective eddy viscosity can be significantly over-predicted, especially for separated flows. This was conducted by comparing RANS, DES, and LES type modelling techniques for a flow over a flat plate at high angles of incidence. This agrees with observations made by Waldmann et al [4], as turbulent viscosity ratios (ν_t/ν) are modelled to be 40 times greater than in DDES solutions. This inflation in effective viscosity ($\nu + \nu_t$) affects momentum transport, which is responsible for the increased wake velocity recovery rate.

Flight regimes are also compounded with dynamic conditions that are neglected under static conditions. Wake characteristics evolve with attitude changes, as the dynamics between attached and separated flow induces further unsteadiness. The computation of dynamic pitch characteristics of a generic transport aircraft are conducted with URANS techniques (SA and k-ω SST) [9, 10]. While recommending a numerical strategy for quantifying numerical convergence in forced pitching cases, it is reported that the choice of turbulence model has a greater impact than grid refinement levels, especially at post-stall angles-of-attack [9]. At $\alpha_0 = 24°$, observations are consistent with separate studies [11] where inadequacies in the RANS models are amplified with larger flow separation. As forced harmonic motion is achieved through mesh dynamics, the suggested approach recommends that the total number of solution iterations per aircraft pitch cycle should be kept equal across cases. This is taken as the product of the number of time-steps per oscillation cycle and number of iterations per time-step [9, 10]. In addition, a grid sensitivity study was conducted across three refinements demonstrating grid independence for lift and pitching moments, but details on the grid design and resolution, in particular the wake region, are ambiguous. Among forced pitch oscillation cases, DES methods proved to be advantageous for higher angles-of-attack [11]. However, Frink [10] comments that their proposed strategy is unlikely to be applicable for such turbulence modelling techniques. One potential reason is the requirement for sufficiently refined temporal and spatial scales in addition to a physically meaningful total solution time frame. This might require increasingly large wake refinement regions coupled with minuscule time-steps, which could cause the proposed approach to be computationally prohibitive.

So far, these work on dynamic pitch simulations have not focused on the effects of wing-tail interaction, especially for conventional aircraft geometry [9]. This is a significant, as wing wake effects must be considered during the pitching manoeuvre. This is in contrast to work by Waldmann et al. [4], Lutz et al. [12], and Gansel et al. [13] where adequate treatment of the near-wake is conducted, although for a *static* case at similar angles-of-attack. This lack of attention on the tail's aerodynamic interactions with the wing wake is also highlighted by Gansel et al. [14] citing concerns for the

computational modelling of transport aircraft configurations dealing with turbulent fluctuations in the wake with regards to the tail [15, 16].

The work detailed in this paper provides an insight on wake interactions between bodies experiencing forced harmonic motion. These dynamics induce flow behaviours and wake interactions that cannot be accomplished under static conditions. To achieve this, a wing-tail configuration in tandem experiencing dynamic pitch is used. The motion of the bodies are coupled, relative to a single rotation centre, representative of an aircraft undergoing pitch oscillations. This reveals any dominant interactions between wing wake-tail dynamics. The harmonics of the problem also enables dynamic flow phenomena to be studied where an oscillating wing wake transitioning between attached and separated flow from pitch is expected. The wake is expected to interact with a tail geometry downstream which experiences a coupled pitch/heave motion as a result of its tail moment arm. The resulting aerodynamics at the tail due to the wake is a function of several components in a dynamic system. Namely, its physical motion relative to the rotational centre with its tail length, the freestream flow conditions affecting wing wake properties, together with the reduced frequency of the harmonic system. These ultimately affect the phase and position of the tail relative to the wake throughout the pitch motion.

III. Simulation Methodology for Dynamic Pitching

The flow conditions are set at $Re_c = 2.14 \times 10^4$ relative to the wing chord, referencing standard sea-level conditions, assuming fully turbulent, incompressible, isothermal conditions of the Navier-Stokes equations:

$$\frac{\partial u_i}{\partial x_i} = 0, \tag{1a}$$

$$\frac{\partial u_i}{\partial t} + u_j \frac{\partial u_i}{\partial x_j} = -\frac{1}{\rho}\frac{\partial p}{\partial x_i} + \nu \frac{\partial^2 u_i}{\partial x_j \partial x_j}. \tag{1b}$$

The equations in the general form are discretised with schemes that are nominally second-order accurate. Spatially, the divergence terms are discretised with a blended central-upwind differencing scheme (CD-UD) [17]:

$$\phi_f = (1-\gamma)(\phi_f)_{UD} + \gamma(\phi_f)_{CD}, \tag{2}$$

where discretisation of the arbitrary primitive variable ϕ is blended with the coefficient γ, weighted at 0.75. As boundedness is not guaranteed with central differencing, an upwind-blended scheme provides boundedness resulting in better numerical stability and accuracy. Time discretisation is achieved with a second-order implicit, backward-differencing scheme [18], where,

$$\frac{\partial \phi}{\partial t} = \frac{\frac{3}{2}\phi^n - 2\phi^o + \frac{1}{2}\phi^{oo}}{\Delta t}. \tag{3}$$

The DDES formulation is built upon the SA model that is based on the correlation of its production and destruction terms in its transport equation [19]. Balancing these gives a relationship that scales the eddy-viscosity with the local deformation rate and distance to the wall. This is analogous to the Smagorinsky model, where it scales with its sub-grid scale eddy-viscosity and grid spacing instead. With this, the distance to the wall in the original SA model is replaced with a hybrid length scale where,

$$\tilde{d} \equiv d - f_d \max(0, d - C_{DES}\Delta), \tag{4a}$$

with

$$f_d \equiv 1 - \tanh([8r_d]^3), \qquad r_d \equiv \frac{\nu_t + \nu}{\sqrt{U_{ij}U_{ij}}k^2 d^2}, \tag{4b}$$

as $f_d = 0$ yields RANS and LES modes for the hybrid length scale. The C_{DES} constant is calibrated at 0.65 [19]. This hybrid formulation allows a RANS-like behaviour and a Smagorinsky-like LES model that switches depending on the proportions between the distance to the wall and local grid spacing. The sub-variant used here is the Delayed-DES (DDES) model which provides an adjustment to the definition of the hybrid length scale that narrows the region of uncertainty between RANS and LES modes (Eq. (4a)). This improved variant has been demonstrated to perform more accurately for separated flows [19].

To achieve dynamic grid motion, the overset method is used to translate the respective sub-grids for the wing and tail geometries in time. The pitch oscillations for angular displacement are described using simple harmonic motion, where,

$$\Delta\alpha(t) = \alpha\cos(\omega t - \phi), \tag{5}$$

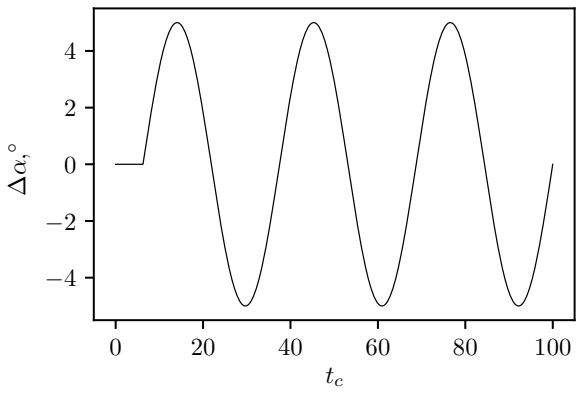

Fig. 1 Three-cycle forced harmonic pitching motion induced to the wing-tail configuration of 5° in addition to its nominal angle-of-attack, at 1 Hz. A flow development time of $6.25t_c$ is allowed before mesh motion occurs.

with the output with respect to convective time illustrated in Fig. 1. The complete mesh motion for the total simulation time is then provided as a look-up table, which allows up to 6-DOF to be described at each time-step for the complete harmonic motion of the overset grids. In the present case only pitch will be considered. Prior to the motion, an initial angle-of-attack offset of $\alpha = 5^\circ$ is imposed in the meshing stage, and a time of $\phi = 6.25t_c$ is given for the flow to develop given uniform initial conditions. Velocity and pressure contours for this developed flow after $6.25t_c$ is shown in Fig. 2. Following this instant, forced harmonic pitching begins at a frequency of 1 Hz resulting in a reduced frequency of 0.1 and is allowed to undergo a total of three cycles.

Due to the large gradients induced from the mesh motion, a wider range of flow Courant numbers are expected compared to static conditions as seen in $t_c \leq 6.25$. The PIMPLE algorithm is used [20], coupled with a Co-based adjustable time-stepping method that is limited to a $Co_{max} < 4$. This is calibrated for computational efficiency accounting for the minute cells along the trailing edges of the wing and tail boundary layer grids. In spite of this, the average $Co \leq 1$ throughout the solution domain. The strategy proposed by Frink [10] and Thompson et al. [9] suggests tracking the number of solution iterations per harmonic cycle to establish numerical convergence is only valid for constant time-stepping solutions. As an adaptive time-stepping technique is used here, the outlined strategy is unsuitable for the present case. Adopting such an approach would be computationally inefficient from the large range of cell sizes present in the domain, and a too large of a time-step size would cause temporal resolution to decrease to unacceptable levels. To overcome this, the first pitch cycle is closely monitored and the numerical tolerances are calibrated to allow an adequate amount of iterations for convergence across this initial phase. This results in total number of iterations that ensures numerical convergence, but with a slight compromise in computational efficiency.

A. Overset Grid Methodology for Forced Harmonic Motion

The wing-tail geometry consists of two 3-dimensional NACA0012 rectangular wings in tandem with an aspect ratio that spans the domain width. To represent a conventional wing-tail configuration, the chord of the downstream NACA0012 tail is reduced to 70% of the front (main) wing chord ($C_{tail} = 0.7C_{wing}$), with a separation distance of $4.28x/C_{MAC}$. This separation distance is based on typical tail lengths suggested by Silverstein and Bullivant [5]. There is no vertical displacement of the tail relative to the wing chord line, and both wing and tail are at 0° incidence to the freestream when levelled.

The individual overset grids for the wing and tail are superimposed over a background grid that defines the overall computational domain, making this a 3-part mesh (Fig. 3). Cell clusters that provide the wing wake refinement region is accomplished with the background mesh as illustrated in Fig. 3a. The local cells in this refinement region are set to $\Delta_{wake} \approx 0.05C_{MAC}$. This domain is adjacent to the oncoming freestream, but the relative position of the tandem configuration is rotated at a $\alpha_0 = +5^\circ$ pitch up clearly seen in Fig. 3b. The forced harmonic motion then amounts to a nominal angle-of-attack of $\alpha = 5^\circ$ with a $\Delta\alpha(t) = \pm 5^\circ$ pitch amplitude about the wing quarter chord point. This results in the wing undergoing pitch oscillations about $0.25C_{MAC}$ exclusively, while the tail experiences a coupled pitch-heave motion due to its moment arm.

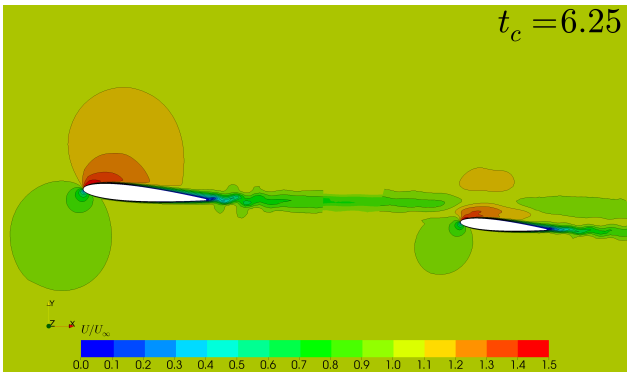

(a) Freestream-normalised velocity magnitude (U/U_∞)

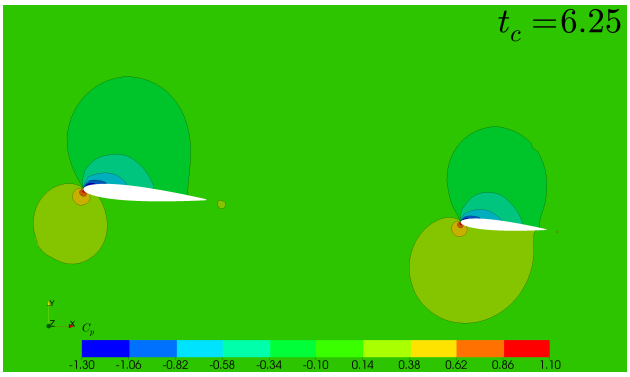

(b) Pressure coefficient contours (C_p)

Fig. 2 The initial flow condition after a flow development time of $6.25t_c$ with a nominal angle-of-attack of $5°$.

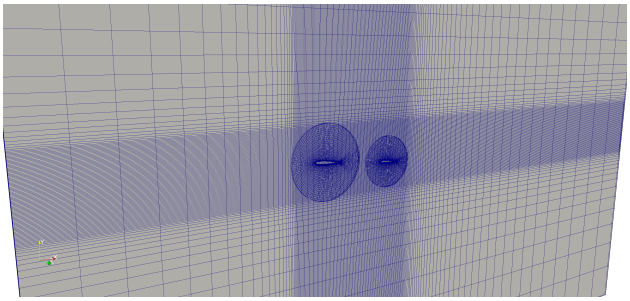

(a) Domain overview

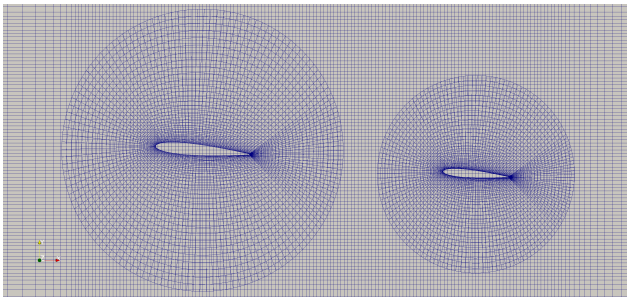

(b) Close-up view of the wing-tail configuration

Fig. 3 Overset grid overview of the wing-tail configuration onto a background grid with localised grading concentrated towards the wake region. Centre of rotation occurs about $0.25C_{MAC}$.

For the overset grid, the definition of different cell zones have to be defined to allow the continuous transport of variables through the domain. The distinction in these zones is illustrated in Figs. 4 and 5, highlighting the different allocated cell types. These are regions containing empty/blocked cells that represent the geometries (red), the interpolation fringes (green), and the background mesh (blue). The wing and tail sub-mesh zones bounded by their respective interpolation fringes are sized at a radius of $1.5C$ from their respective mid-chords. The interpolation fringes do not overlap with this sizing and separation distance for the two sub-meshes. The status of these cells types (empty, background, interpolation fringe) ensures domain connectivity and their coupling [21].

Fringe interpolation uses the Inverse Distance scheme [22], where the weighted average is based on the distance between the interpolation and donor cell centres. The general form of the interpolation function for obtaining an interpolated value $\tilde{\phi}$ at a given point x is defined with:

$$\tilde{\phi}(x) = \frac{\sum_{i=1}^{N} w_i \phi(x_i)}{\sum_{i=1}^{N} w_i}, \tag{6}$$

where the weight corresponding to the i-th donor cell,

$$w_i = \frac{1}{|x - x_i|^P}, \tag{7}$$

with x_i as the known point to distance to x. This is summed up over N, which is the total number of points used in the interpolation with P as the power parameter constant [23]. As the weight in Eqn. 7 is inversely proportional to the distance between the interpolated points, the discrete time-step size affects the arbitrary distance between cells at each time-step. Thus, the mesh motion introduces an additional simulation control parameter known as a *mesh* Courant number. Analogous to the *flow* Courant number, this defines the motion of the sub-zone meshes relative to each other. This criteria ensures that an adequately refined time-step size satisfies the desired temporal resolution with regards to mesh movement to support interpolation at the fringes. This has to be considered in addition to the flow field on the static grid. Ideally, the ratio between the mesh and flow Courant numbers should be maintained at unity throughout the range of motion conducted in the simulation.

A visualisation of the wing and tail sub-zone meshes relative to the background mesh is depicted in Fig. 5. Here, the wing and tail sub-zone grids are overlaid on to the background mesh highlighted with different cell types. The background grid is designed to account for approximately four to six empty cells (red) along the thickness of the geometries, with the interpolation fringe (green) for the walls. This ensures that an appropriate background grid definition is given for the geometries, especially for the tail (Fig. 5b), where the largest movements are expected.

Based on the initial flow development time, the boundary layer grid of both geometries result in a dimensionless first cell height of $y^+ = 1$ growing at a rate of 1.05, ensuring adequate viscous sublayer treatment. For a given aspect ratio, cell sizes in the lateral directions correspond to $x^+ \approx 90$ and $z^+ \approx 90$. For this described grid design, the total grid points in the domain amount to approximately 650k cells for all elements in this 3-part mesh. This is kept economical while uncompromising on the solution integrity in terms of wake refinement ($\Delta_{wake} \approx 0.05C_{MAC}$) as mesh motion can be computationally expensive.

A comparison of cases involving forced pitch oscillations, including the present case, are as summarised in Table 1. Of these, only one considers the use of a DDES for dynamic pitch. However, the case by Hall et al. [11] is performed on a BWB geometry which lacks an empennage assembly and is therefore slightly beyond the scope of focus in this work, which emphasises on tail aerodynamics. Most of the simulation parameters are comparable although Mach number is likely to have been determined by wind tunnel test specifications for the other cases. The present results are based only on the DDES turbulence modelling technique coupled with an adaptive time-step based on the instantaneous Courant number during solution run-time. This is in contrast to what is used by Frink [10] and Thompson et al. [9] with a constant time-step. The use of DDES also complements these work as it provides the resolution necessary for capturing wake turbulence that cannot be achieved with RANS.

IV. Wing-Tail Behaviour in Forced Harmonic Pitch

The following analyses presents results for the flow over the wing-tail geometry in forced harmonic pitch oscillation. This is conducted at the described motion of $\alpha(t) = 5 \pm 5^\circ$ at $k = 0.1$ that is comparable to the other cases listed in Table 1 with the exception of the Reynolds number while still within an incompressible regime. The general observation in the resulting solution shows that as the tandem configuration oscillates, the tail pitches and heaves in and out of the

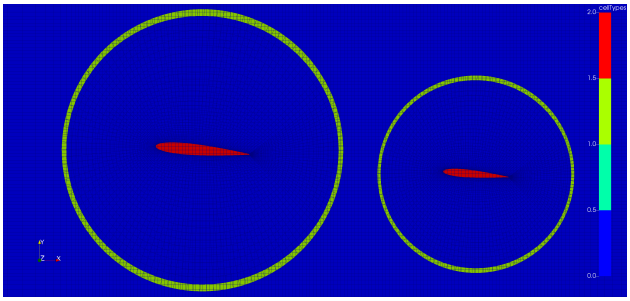

(a) Wing tail sub-zones with outer interpolation fringes

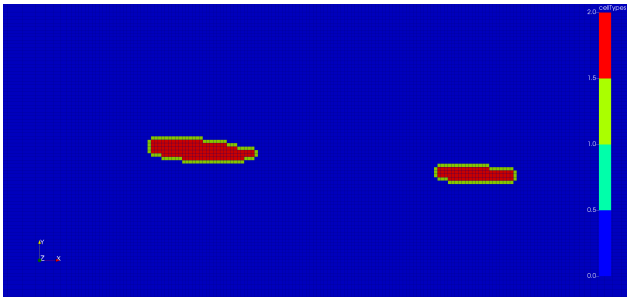

(b) Wing tail grid with wall fringes

Fig. 4 Overset grid of the wing-tail configuration with the background mesh (blue) highlighting the boundaries of overset cell types (red: empty cells, green: interpolation fringe, blue: background mesh).

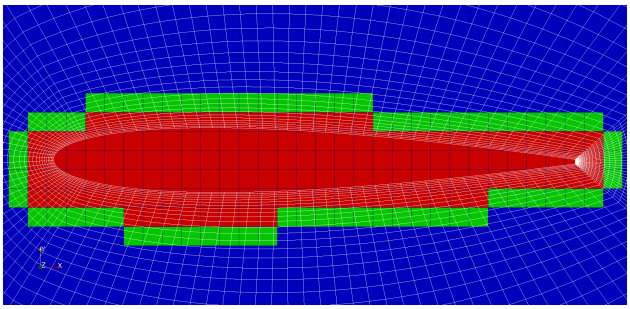

(a) Wing boundary layer grid

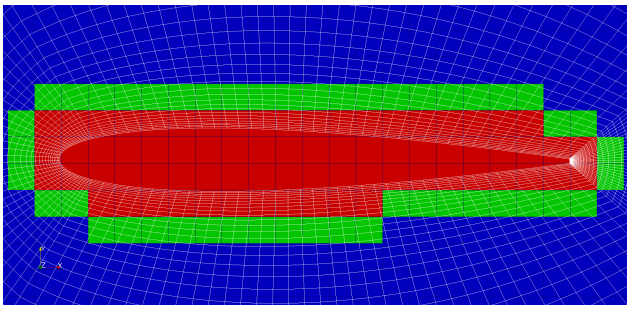

(b) Tail boundary layer grid

Fig. 5 Both wing and tail boundary layer grids superimposed over the background grid illustrating the contrast in different cell zone sizes (red: empty cells, green: interpolation fringe, blue: background mesh). Note the number of cells that define each region.

Table 1 Comparison of reviewed forced pitching oscillation cases, including the present case, comparing flow parameters and case set-up.

Case Geometry	Flow cond.	Pitch amplitude	Char. time-step	Reduced freqs.	Turb. models	Cells (million) y^+ at $0.5C_{ref}$
Present case: Tandem NACA0012	2.1×10^4, 0.01	$\Delta\alpha = \pm 5°$ at 5°	Adaptive Co-based	0.1	SA-DDES	0.65 $y^+ = 1$
Hall et al. BWB [11]	7×10^5, 0.1	$\Delta\alpha = \pm 5°$ at 0°, 8°, 16° 24°, 32°	-	0.07	SA k-ω SST SA-DDES	0.7, 4.7, 4.9
Thompson et al. GTM [9]	5.4×10^5, 0.077	$\Delta\alpha = \pm 5°$ at 24°	$\Delta t_c = 0.02$ 1500 time-steps	0.01483 0.00401 0.00167	SA k-ω SST	6, 12, 24 $y^+ = 0.75$
Frink SACCON [10]	1.61×10^6, 0.0144	$\Delta\alpha = \pm 5°$ at 0°, 10°, 15°, 20°	$\Delta t_c = 0.006$ to 0.290	0.06 0.12 0.18	SA k-ω SST	3, 6, 9, 12 $y^+ = 0.5$

wing wake. This induces a periodic interaction that is evident in the force coefficient time-histories. With the wing as the wake generator, the results can be analysed as two separate parts, by focusing firstly on the wing in harmonic pitch motion that is independently assessed from the tail downstream. The conditions of forced pitching also induces flow separation as the wing stalls at the higher, peak angles-of-attack.

Subsequently, the results focus on the tail relative to the wing wake, where the primary contribution lies in advancing the understanding of the tail interaction with its wing wake under these conditions. Key flow features such as its interaction with the wing LEV/TEVs are captured, and presented relative to tail surface pressure distribution as a result of this interaction. As the tail exhibits sinusoidal lift characteristics resulting from heave due to the moment arm, the Theodorsen's function is proposed as a suitable approximation method. However, this neglects the underlying response due to wake encounter, which is observed as distinct variances that deviate along the harmonic response.

Finally, distinct features in the *total* lift response of the tandem system can be attributed to the wing stall and wake interference with the tail that was previously analysed separately. The total contribution by the system can therefore be described as the synthesis of both wing and wake-tail dynamics. This is revealed in the lifting response of the tandem configuration while undergoes this forced pitching manoeuvre.

A. Wing Behaviour in Dynamic Pitch

The characteristic waveform of the force coefficients by the wing undergoing the harmonic pitch cycle are illustrated in Figure 6. The results are shown across 100 convective time-steps, demonstrating its longitudinal forces and pitching moment response. The initial phase of the solution that is allowed to develop at $t_c \leq 6.25$ is reflected in the output, and plateaus to a quasi-steady state before the pitch oscillations begin. This initial phase begins with a pitch up where the effective angle-of-attack gradually increases up to a peak of $\alpha(t) = 10°$. This characteristic spike in lift coefficient is periodic and can be attributed to the hysteresis of the problem, as $dC_L/d\alpha$ decreases toward the maximum angle-of-attack. A stall indicated with a sharp drop in lift follows the decrease in pitch back down to its nominal value and then its trough at $\alpha(t) = 0°$. This is observed to occur for total three pitch cycles.

The hysteresis in the lifting response by the wing is illustrated in Fig. 7. Here, the initialisation portion of the solution becomes more apparent and the stall behaviour relative to angle-of-attack is better represented. The lift curve is clearly defined up to the maximum $\alpha(t) = 10°$ before the flow separates with a corresponding sharp decline in lift. It is apparent that the wing undergoes a complete stall as indicated by its loss in lift coefficient at approximately $\alpha(t) < 9°$ on the downstroke. Throughout this phase, large oscillations in the lift coefficient occur before it begins to settle at approximately 6°. The reattachment of the flow can be better visualised in terms of its flow field, which are depicted in Figs. 8. These are taken across $46.88 \leq t_c \leq 50.00$ with contours of velocity magnitude and pressure coefficient, showing the upper surface flow separation that occurs in this phase. The shedding of the wing LEV/TEV are captured

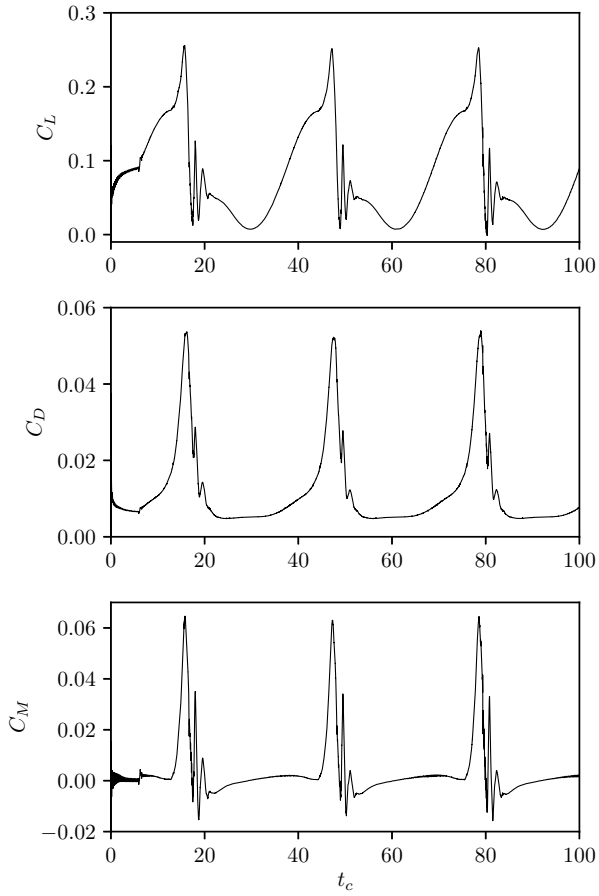

Fig. 6 Wing-only force coefficient time-history resulting from forced harmonic pitching about $0.25C_{MAC}$ **at** $\alpha = 5 \pm 5°$**.**

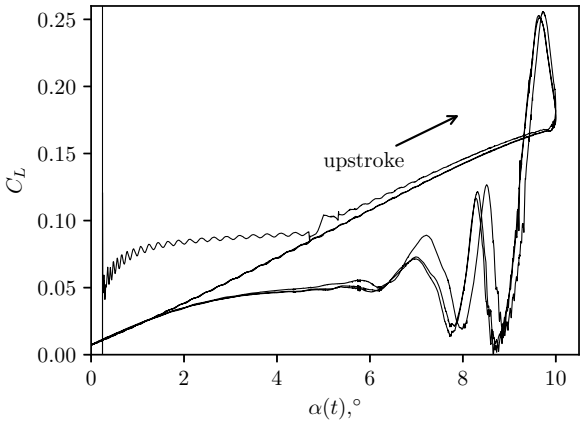

Fig. 7 Hysteresis of wing lift coefficient against angle-of-attack undergoing forced pitch oscillations (three cycles) about $0.25C_{MAC}$ at $\alpha = 5 \pm 5^\circ$, $k = 0.1$.

clearly, identified with low-pressure vortex cores that emanate from the leading and trailing edges of the wing.

Two of the corresponding convective time-steps ($t_c = [46.88, 48.44]$, at $\alpha(t) = [9.75, 9.04]^\circ$) in Figs. 9 show a negative C_p across the entire upper surface of the wing. This is characteristic of a complete wing stall, with the effects of the LEV convecting over the upper surface of the wing captured with a suction peak in negative C_p at approximately $0.75x/c$ (Fig. 9a). This same effect is repeated at $t_c = 48.44$ (Fig. 9b) as the LEV detaches from the top surface of the wing. However, the LEV and TEV in this instant nearly coalesce toward the trailing edge as depicted in Fig. 8d. The influence of this larger low pressure vortex core is evident in Fig. 9b as a large suction magnitude of up $C_p = -3$ can be seen.

As the wing undergoes this harmonic pitch oscillation, its response due to this motion can be approximated with the Theodorsen's function [24] for the estimation of unsteady loads that is based on reduced frequency where:

$$C(k) = \begin{cases} 1 - \dfrac{0.165}{1 - \dfrac{0.045}{k}j} - \dfrac{0.355}{1 - \dfrac{0.30}{k}j}, & k \leq 0.5, \\ 1 - \dfrac{0.165}{1 - \dfrac{0.041}{k}j} - \dfrac{0.355}{1 - \dfrac{0.32}{k}j}, & k > 0.5. \end{cases} \tag{8}$$

with the lift response:

$$L = \pi\rho b^2 \left[\ddot{z} + U_\infty\dot{\theta} - ba\ddot{\theta}\right] + 2\pi\rho U_\infty bC(k)\left[\dot{z} + U_\infty\theta + b(\tfrac{1}{2} - a)\dot{\theta}\right], \tag{9}$$

where $z = z_0 e^{i\omega t}$ and $\theta = \theta_0 e^{i\omega t}$ for oscillatory heave and pitch displacements, respectively.

The results obtained in this section can therefore be partially verified knowing the harmonic pitch characteristics of this predetermined wing motion. Figure 10 shows the Theodorsens's approximation in comparison with the wing lift response as a result of forced harmonic pitch oscillation. Note that the sinusoidal function has been corrected to account for flow development time and nominal lift coefficient at ($\alpha_0 = 5^\circ$). The result and the empirical approximation compares well, where both amplitude and phase correspond to the computational results, especially during the pitch-up phases (positive $dC_L/d\alpha$). However, this is with the exception that the function is unable to capture the stall characteristics of the wing. This limitation in the Theodorsen's function agrees with what is reported by Cordes et al. [25] and Amiralaei et al. [26], where it is only limited to moderate angles-of-attack without flow separation.

Apart from the wing response, the additional key feature for verification is in its wake. While the wing undergoes a harmonic motion, its wake characteristics change with angle-of-attack. Instantaneous data will not be physically meaningful, while time-averaging is invalid as a large range of spectral content is present in addition to constantly changing grid points. As a result, conducting statistical analyses for the present wake data is challenging. For these reasons, analyses for the wing response is only measured against the Theodorsen's function as a validation metric, and the outcome supports the reported wing behaviour as shown in Fig. 10.

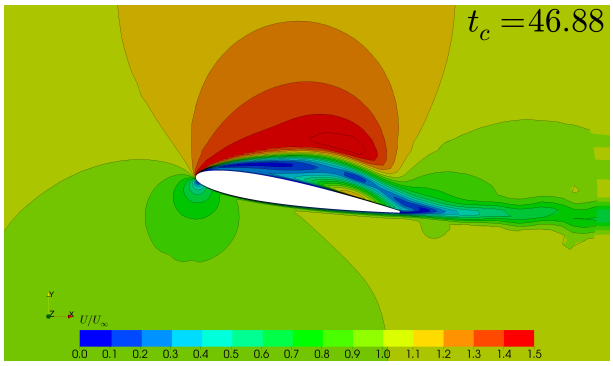

(a) Velocity magnitude, $t_c = 46.88$**,** $\alpha(t) = 9.75°$

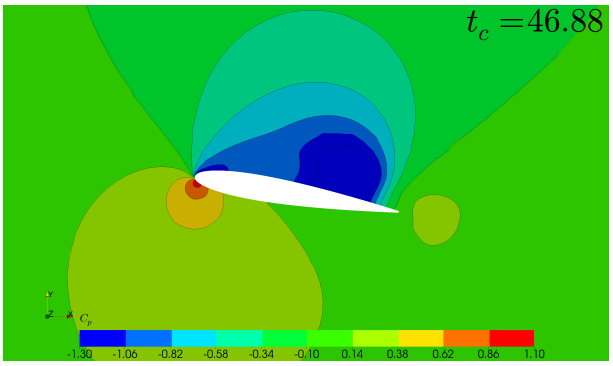

(b) Pressure coefficient, $t_c = 46.88$**,** $\alpha(t) = 9.75°$

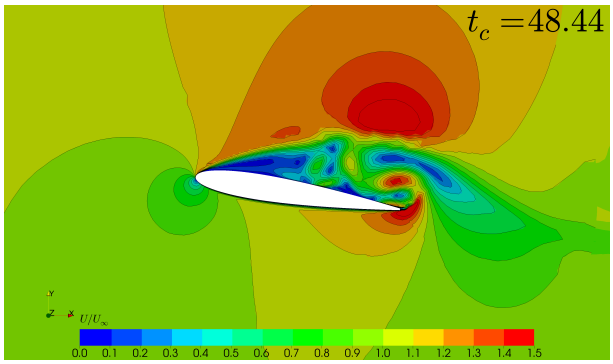

(c) Velocity magnitude, $t_c = 48.44$**,** $\alpha(t) = 9.04°$

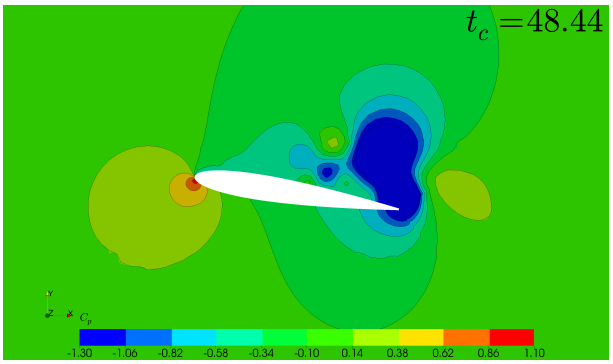

(d) Pressure coefficient, $t_c = 48.44$**,** $\alpha(t) = 9.04°$

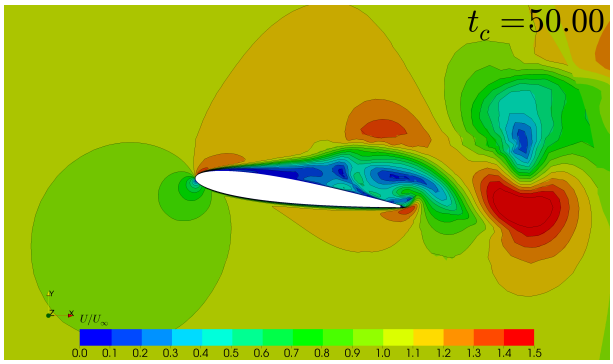

(e) Velocity magnitude, $t_c = 50.00$**,** $\alpha(t) = 7.93°$

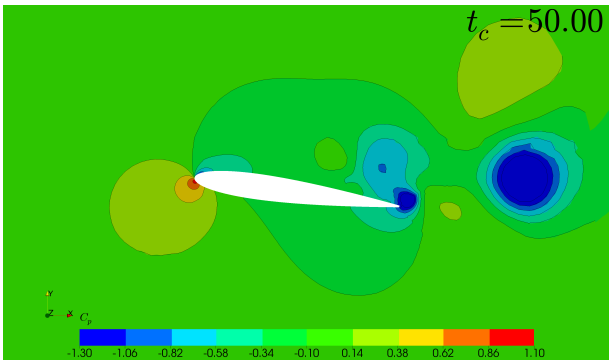

(f) Pressure coefficient, $t_c = 50.00$**,** $\alpha(t) = 7.93°$

Fig. 8 Freestream-normalised velocity contours (U/U_∞) **and its corresponding pressure coefficient** (C_p) **around the wing at** $t_c = [46.88, 48.44, 50.00]$**.**

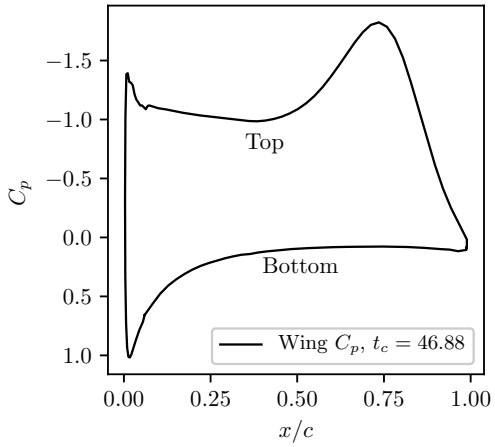

(a) $t_c = 46.88$**,** $\alpha(t) = 9.75°$

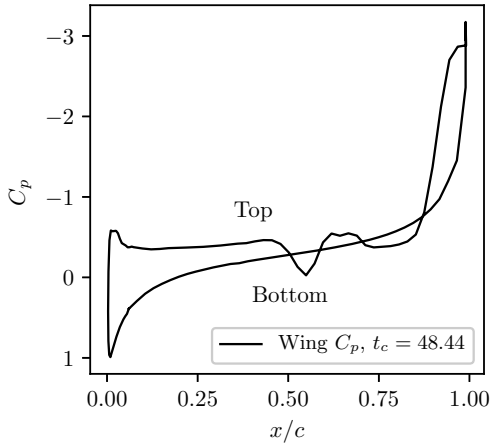

(b) $t_c = 48.44$**,** $\alpha(t) = 9.04°$

Fig. 9 Instantaneous pressure coefficient across the wing at $t_c = [46.88, 48.44]$**.**

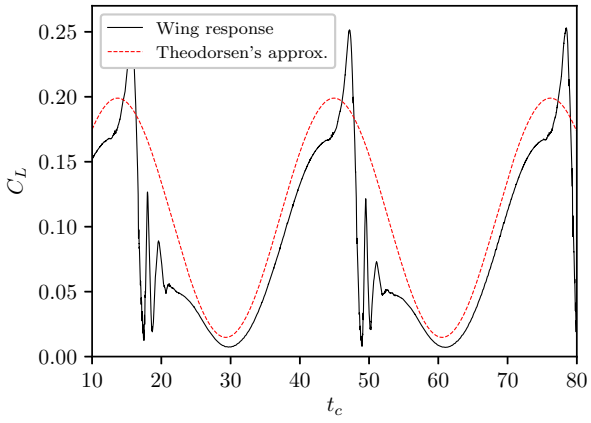

Fig. 10 Comparison of the wing lift response to the Theodorsen's approximation symmetric airfoils undergoing harmonic pitch.

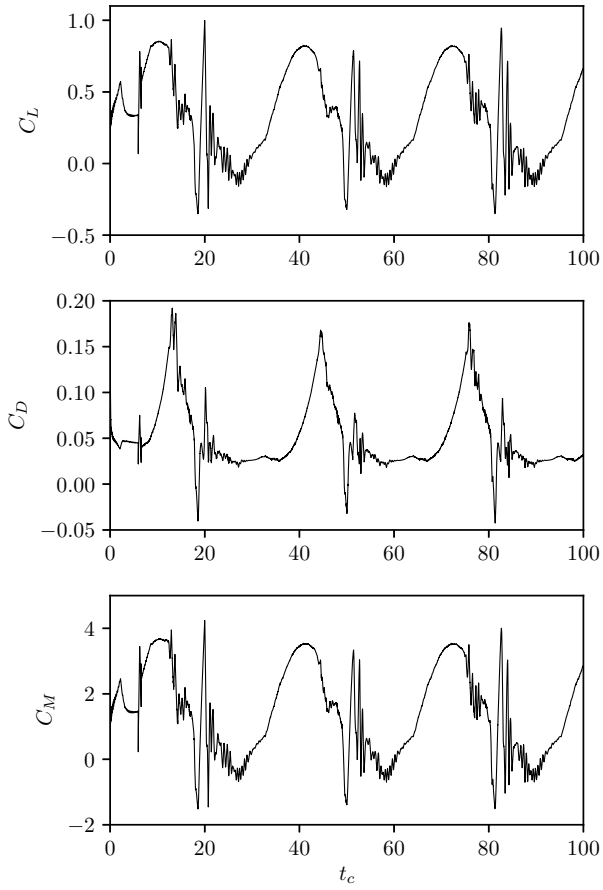

Fig. 11 Tail-only force coefficient time-history resulting from forced harmonic pitching about $0.25C_{MAC}$

B. Tail Behaviour Subjected to Wing Wake

The tail response in terms of its force coefficient time-histories is illustrated in Fig. 11. The tail undergoes a motion that is similar to its wing, with the exception of the tail moment arm that contributes to a heave. As the motion of both wing and tail are coupled with identical angle-of-attack relative to the freestream, the tail lift response exhibits similar sinusoidal waveform characteristics including the large variances evident during the negative $dC_L/d\alpha$ sections in the force history. Similarly to the wing, flow separation may be responsible for such a behaviour but the variances in the tail moments also reveal the influence of the wing wake.

The magnitude of these variances exceed the sinusoidal peaks of the tail response which are presented in terms of $\alpha(t)$ in Fig. 12. It becomes more apparent that as the geometry pitches up, the tail plunges out of wing wake influence, providing a relatively distinct lift curve up to the maximum of $\alpha(t) = 10°$. The stall characteristics decreases the lift coefficient slightly as the configuration pitches back down. At this instant, the effects of the wing wake begin to manifest as large variances in the tail lift response. The occurrence of this phenomenon depends on the convective time of the wake relative to the tail length, but at present these large amplitudes reveal themselves at $4° \leq \alpha(t) \leq 7°$. The oscillations begin to settle as the configuration approaches its trough at $\alpha(t) = 0°$ and the tail resides in the attached wing wake. These phases of the pitch cycle showing the effects of wake interaction are important to distinguish wake interactions at the tail.

As a result of the configuration pitching down, the tail heaves into the currently separated wing wake. The sequence of flow events that captures this interaction that occurs between $4° \leq \alpha(t) \leq 7°$ can be better visualised using Figs. 13 to 16. Figure 13 illustrates the instantaneous flow in terms of pressure coefficient. The wing LEV and TEV low pressure vortex cores are clearly identifiable. However, determining the source of these vortices requires the aid of vorticity contours where the span-wise component (ω_z) is shown in Fig. 14. This distinguishes the rotational direction

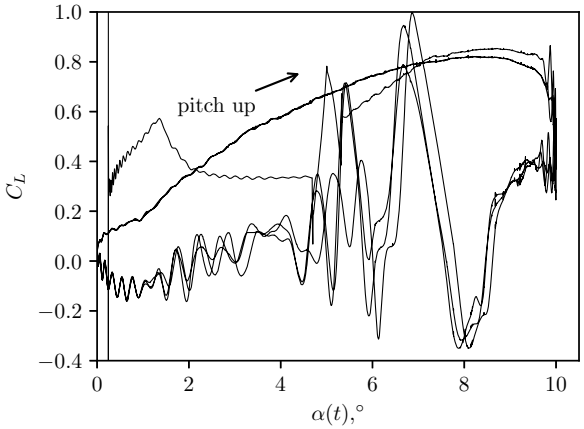

Fig. 12 Hysteresis of tail lift coefficient against angle-of-attack. The depicted hysteresis consists of three forced harmonic oscillations about $0.25C_{MAC}$ ($\alpha(t) = 5 \pm 5°$, $k = 0.1$).

and origins of the individual vortices. This shows that the wing trailing edge sheds a dominant vortex compared to the leading edge, which convects over the system. This is expected as the pitch centre of the geometry is farther from the trailing edge ($0.25C_{MAC}$).

Details of this flow sequence are revealed between $51.25 \leq t_c \leq 51.88$ (Figs. 13c to 13e) as the wing TEV coincides with the tail while it heaves into the wake. The wing TEV convects downstream, which almost coalesces with the tail LEV pictured in Fig. 13d. However, their counter-rotation prevents this from occurring based on the sign of the vorticity component shown in Fig. 14d). As this wing TEV now convects farther downstream and over the tail, its low pressure core is observed to affect tail loads. This effect can be inferred from results showing instantaneous pressure coefficient distribution in Fig. 15 manifested as low pressure suction peaks. These peaks convect across $0.25C_t$ over the top surface within approximately $0.32t_c$. This corresponds to the large variances in tail loads as shown previously in Fig. 11. While this observation for the wing TEV relative to the tail may be unique to this reduced frequency, the contours presented so far provide some insight to the understanding of this wake interaction, which also encompasses some extent of flow separation at the wing.

To further support the validity of the solution, the effects of turbulent viscosity ratio is shown in Fig. 16. Peak viscosity ratios at approximately $15\nu_t/\nu$ that lie within the low pressure vortex cores are depicted. This provides an indication of the rise in turbulent transfer of energy as a result of the moving eddies in the wake, which relates to higher stresses in the flow. However, the dynamic grid makes analyses beyond the instantaneous results challenging, especially for averaging statistics. Time-averaging a dynamic overset grid does not provide physically meaningful results as the discrete location of grid points are time-dependent. Statistical analyses in the wake like turbulent length scales and its stresses with regards to the tail would allow these effects to be better quantified. Nevertheless, comparing the results between the wing and tail reveals a degree of correlation between their individual responses. Because of the wake, a correlation between their respective lift coefficients can be inferred. This is supported with a pairwise correlation coefficient of 0.92, which is a strong indicator of the inter-dependence between the two geometries. While the coupled motion of the configuration contributes heavily to this correlation, the slight phase lag can be attributed to the tail moment arm with heave at the tail, inducing an even greater degree of unsteadiness in the system. These observations support the inferrences made by Waldmann et al. [2] under static conditions for wing-tail correlations regarding the phase lag by the tail moment arm.

Similar to the wing, the tail response is verified with the Theodorsen's function shown in Fig. 17. In contrast to the wing pitch-exclusive dynamics, the tail experiences heave as a result of its moment arm from the rotational centre. Knowing the total pitch angle (10°) with its tail length gives an estimation for its heave amplitude. The result of this is also a sinusoidal function that is corrected for its nominal $C_L(\alpha)$. Ignoring the large variances due to the wake interference, the Theodorsen's approximation fits the tail response very well. In addition, the tail does not appear to exhibit the same stall characteristics compared to the wing. Other irregularities in terms of smaller variances are also present in the negative $dC_L/d\alpha$ regions but this is indistinguishable between wing wake interference or tail stall. However, examining the tail pressure coefficient distribution also do not reveal the involvement of significant tail stall

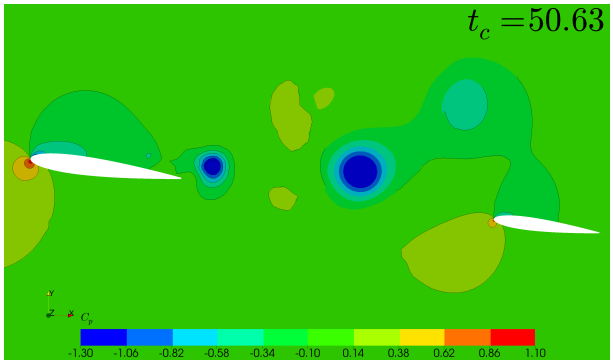

(a) t_c = 50.63, $\alpha(t)$ = 7.41°

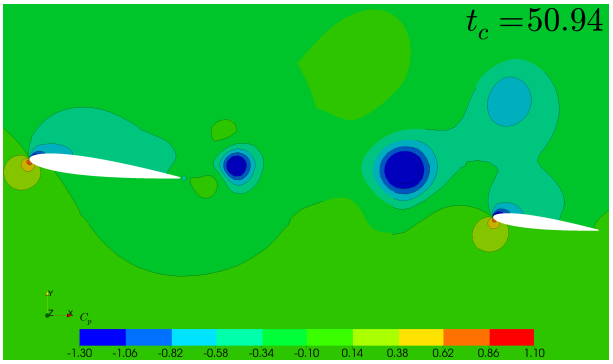

(b) t_c = 50.94, $\alpha(t)$ = 7.13°

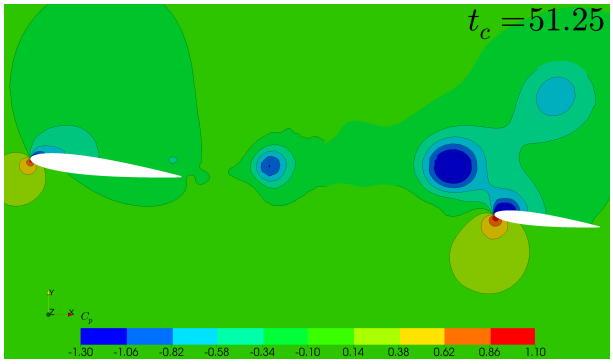

(c) t_c = 51.25, $\alpha(t)$ = 6.84°

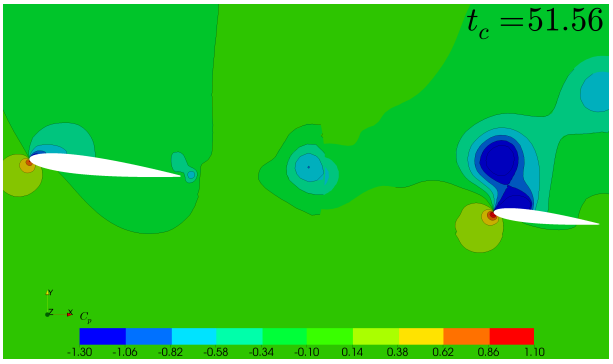

(d) t_c = 51.56, $\alpha(t)$ = 6.55°

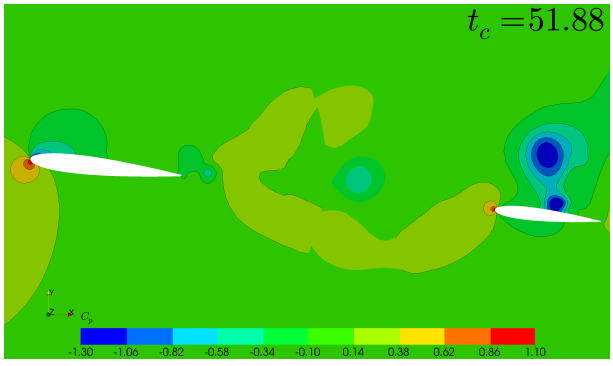

(e) t_c = 51.88, $\alpha(t)$ = 6.24°

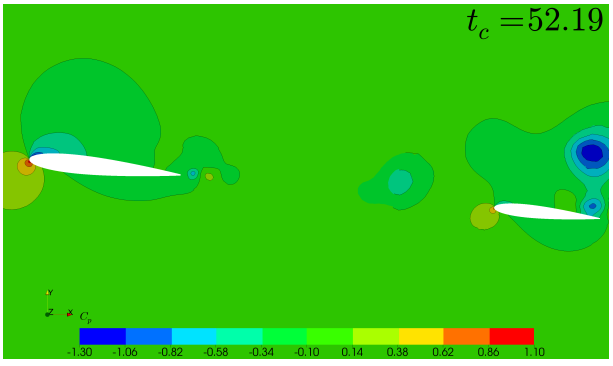

(f) t_c = 52.19, $\alpha(t)$ = 5.94°

Fig. 13 Pressure coefficient (C_p) contours showing the convection of wing LEV and TEV relative to the tail across $1.56t_c$. LEV and TEV low pressure zones (in blue) are clearly identifiable (Configuration pitching down).

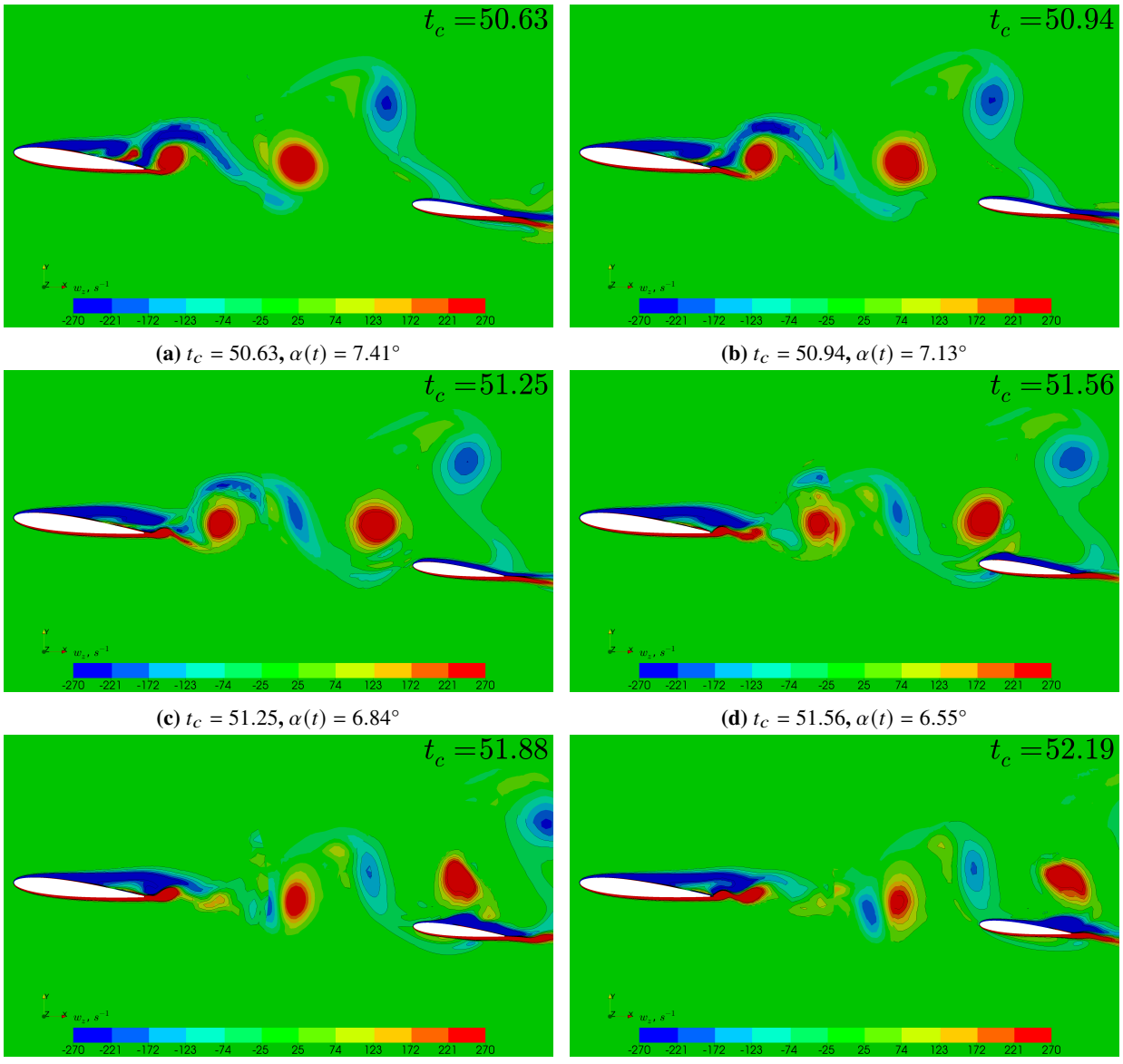

(a) t_c = 50.63, $\alpha(t)$ = 7.41°

(b) t_c = 50.94, $\alpha(t)$ = 7.13°

(c) t_c = 51.25, $\alpha(t)$ = 6.84°

(d) t_c = 51.56, $\alpha(t)$ = 6.55°

(e) t_c = 51.88, $\alpha(t)$ = 6.24°

(f) t_c = 52.19, $\alpha(t)$ = 5.94°

Fig. 14 Span-wise vorticity contours (ω_z) showing the convection of wing LEV and TEV (Red; counter-clockwise, Blue; clockwise) relative to the tail across $1.56t_c$ (Configuration pitching down).

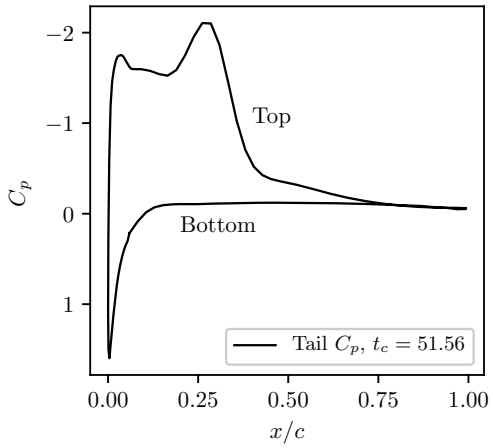

(a) t_c = 51.56**,** $\alpha(t)$ = 6.55°

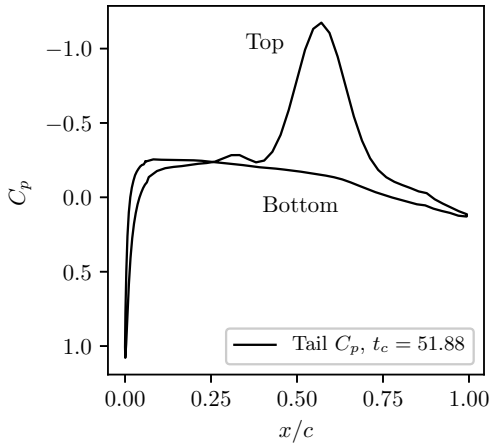

(b) t_c = 51.88**,** $\alpha(t)$ = 6.24°

Fig. 15 Instantaneous pressure coefficient across the tail with the wing wake passing over its top surface as a low pressure suction peak.

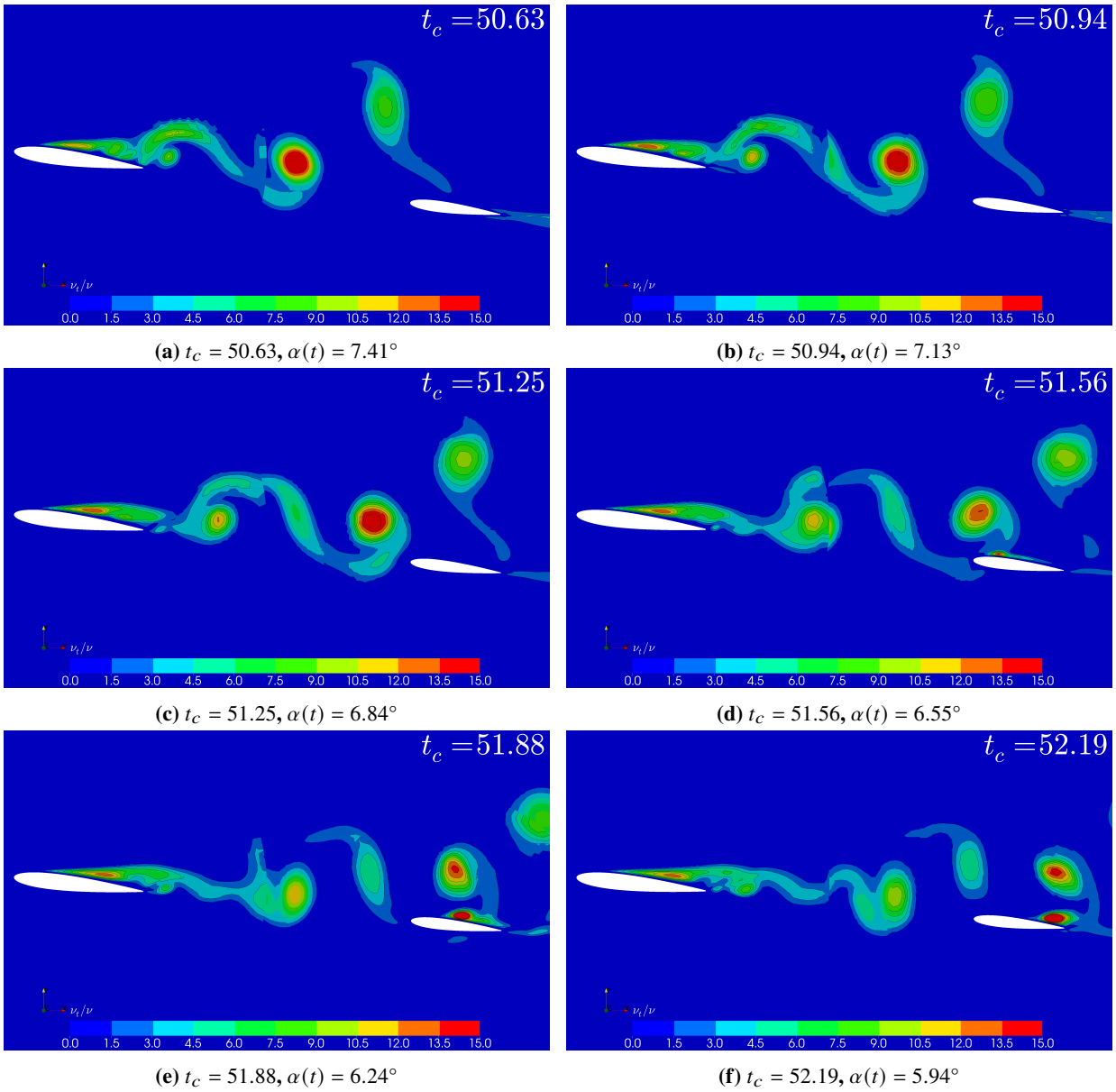

(a) $t_c = 50.63$, $\alpha(t) = 7.41°$ **(b)** $t_c = 50.94$, $\alpha(t) = 7.13°$

(c) $t_c = 51.25$, $\alpha(t) = 6.84°$ **(d)** $t_c = 51.56$, $\alpha(t) = 6.55°$

(e) $t_c = 51.88$, $\alpha(t) = 6.24°$ **(f)** $t_c = 52.19$, $\alpha(t) = 5.94°$

Fig. 16 Turbulent viscosity ratio (ν_t/ν) showing the convection of wing LEV/TEV relative to the tail across $1.56t_c$ (Configuration pitching down).

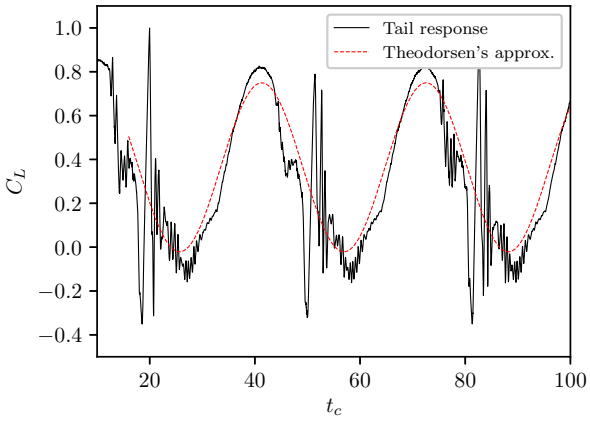

Fig. 17 Comparison of the tail lift response subjected to wing wake interference to the Theodorsen's approximation symmetric airfoils undergoing coupled pitch and heave.

dynamics. Based on these, the dissimilar tail stall characteristics despite sharing an identical angle-of-attack with the wing is likely due to the effects of local Reynolds numbers. As the tail is sized to 70% the wing chord, it perceives different local flow conditions, in addition to a region of reduced velocities induced by the wake. This causes different local flow conditions which may alter stall characteristics. The hysteresis caused by the heave motion may also have contributed to this, but this is a function of reduced frequency and can only be determined with differing dynamic conditions of the study.

C. Synthesis of Force Contribution by Both Wing and Tail

Results so far have treated the wing and tail individually. As this is a coupled system, their significance therefore lies in the synthesis of all components (wing and tail) for the total response of the tandem configuration. Figure 18 shows this in terms of its force coefficients, with the system taken as a coupled whole. Here, the lift characteristics encompasses distinct features that can be explained considering the aforementioned discussions for the wing and tail.

Figure 19 singles out a pitch cycle for the lift coefficient of the entire system. Following what was discussed, two distinct features can be highlighted from this response. Assuming that the wing contributes to the majority of the lift, the characteristic “pinch" in the lift coefficient due to hysteresis can be identified. This was apparent before in Fig. 6, and was attributed to wing pitching and stall dynamics. In addition, the decrease in angle-of-attack leads to an interaction between the wing wake and tail. This leads to the second response highlighted in Fig. 19 where the wake affects the tail. Although the phase and amplitude of this interaction are highly dependent on reduced frequency, the present conditions allow these features to be distinguishable, and demonstrate the aerodynamic coupling that occurs between the two geometries.

So far, the breakdown of components have been captured and analysed as part of this chapter. The results and observations agree with mechanics outlined by Etkin and Reid [1] where the total behaviour of the system lies in the contribution of individual systems. In the present case, this is limited to the dominant contributors of lift–and therefore moments–which are the wing and tail. Furthermore, their correlations are successfully identified and presented through physical phenomena. This advances the observations made by Waldmann et al. [2, 4] where the tail is engulfed by the wing wake only under *static* conditions. Aircraft stability characteristics with dynamic pitch were also studied by Frink [10] and Thompson et al. [9] but local aerodynamic interactions were beyond their scope of work. Wing wake effects were unconsidered as part of their evaluation for pitch stability. Based on this, the current work has filled this gap by providing an insight to wing wake-tail interactions under such forced harmonic pitch conditions.

V. Conclusion

The effects of a wing wake shed downstream onto its tail are demonstrated. The conditions imposed by forced harmonic oscillation inducing wing stall dynamics where the flow detaches and develops into LEV and TEVs. A

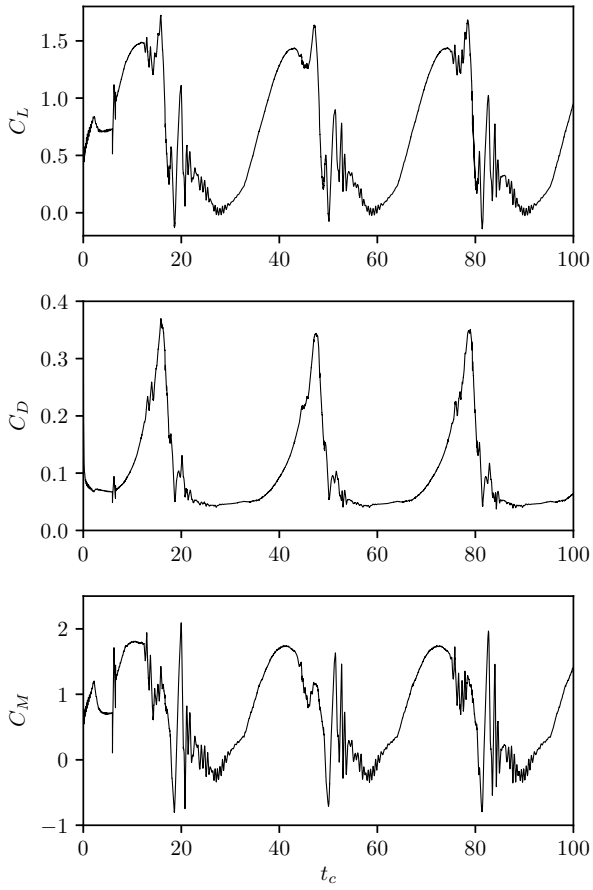

Fig. 18 Total force coefficients for the wing-tail configuration undergoing forced harmonic pitch oscillation.

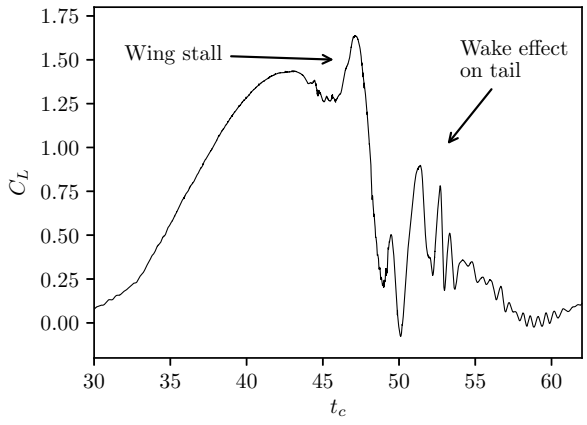

Fig. 19 Close-up of one lift coefficient cycle for the coupled wing-tail configuration undergoing forced harmonic pitch oscillation, highlighting the synthesis of wing stall and its wake effects on the tail.

corresponding separated wake is shed, while the tail experiences a coupled pitch/heave motion due its moment arm. As it heaves and plunges in and out of the wing wake, the tail responds with large load variations, exceeding that of its own maximum lift coefficient from pitch displacement alone. The phase of this phenomenon strongly correlates to the timing of distinct wing wake features that are shed downstream. These features are captured, and identified as wing LEV/TEV pairs, where the TEV is evidently dominant as the rotation centre is imposed at the wing quarter chord point. While vortex cores are inherently low pressure, their effects translate to the tail, evident in its pressure distribution as it heaves into the separated wing wake. Wake effects on the tail are therefore readily apparent, and are distinguishable from stall characteristics. This is evident from correlations drawn between the wing and tail lift coefficient time-histories. The computed tail lift forces show significant variances that strongly relate to those exhibited by the wing, revealing that the source of these are a consequence of wing wake interaction.

As a dynamic motion is induced, the wing response as a result of pitch can be approximated with an empirical approach using the Theodorsen's function for unsteady aerodynamics. Similarly, it is shown that this can be applied on the tail, accounting for heave due to the tail moment arm. However, comparing the tail response with the Theodorsen's function neglects an additional component that accounts for wing wake interference effects. This suggests that the complete tail response including the effects of the wing wake could be approximated with an additional gust component adjusted with phase lag to account for the tail moment arm as a convective length.

This dynamic case has captured the pitch hysteresis while identifying key aerodynamic behaviour. This includes stall dynamics for the wings, where characteristic LEV/TEVs are captured and observed to convect downstream towards the tail. Tail aerodynamics are also shown to respond to the wake, evident through its surface pressure distributions. The harmonic nature of the tail response therefore allows it to be predicted, while discrepancies in the approximation method are attributed to an additional gust component that could be used to account for wake effects. Distinct features in the total lifting response of the system are subsequently revealed to be the synthesis of wing stall and its wake interaction with the tail. These effects prove that wing-wake tail interactions are perceptible by the combined system.

Acknowledgments

The work is funded through the Industrial Postgraduate Programme scholarship by the Economic Development Board of Singapore, in partnership with AviationLearn Pte. Ltd. and the University of Glasgow Singapore.

References

[1] Etkin, B., and Reid, L. D., *Dynamics of Flight: Stability and Control*, chapter and pages, pp. 18–33.

[2] Waldmann, A., Lutz, T., and Kraemer, E., "Separated Wake Flow and Tail Loads of the Common Research Model in Low Speed Stall Conditions," *AIAA Scitech 2019 Forum*, 2019, p. 2315.

[3] Byrnes, A., Hensleigh, W., and Tolve, L., "Effect of Horizontal Stabilizer Vertical Location on the Design of Large Transport Aircraft," *Journal of Aircraft*, Vol. 3, No. 2, 1966, pp. 97–104.

[4] Waldmann, A., Gansel, P. P., Lutz, T., and Krämer, E., "Unsteady Wake of the NASA Common Research Model in Low-Speed Stall," *Journal of Aircraft*, Vol. 53, No. 4, 2015, pp. 1073–1086.

[5] A. Silverstein, S. K., and Bullivant, W. K., "NACA Report 651: Downwash and Wake Behind Plain and Flapped Airfoils," Tech. rep., NACA, 1939.

[6] Lockheed, "Aerodynamic Data for Structural Loads: C-130," , 1953.

[7] Vassberg, J., Dehaan, M., Rivers, M., and Wahls, R., "Development of a Common Research Model for applied CFD Validation Studies," *26th AIAA Applied Aerodynamics Conference*, 2008, p. 6919.

[8] Breuer, M., Jovičić, N., and Mazaev, K., "Comparison of DES, RANS and LES for the Separated Flow Around a Flat Plate at High Incidence," *International Journal for Numerical Methods in Fluids*, Vol. 41, No. 4, 2003, pp. 357–388.

[9] Thompson, J., Frink, N., and Murphy, P., "Guidelines for Computing Longitudinal Dynamic Stability Characteristics on Subsonic Transport," *28th AIAA Applied Aerodynamics Conference*, 2010, p. 4819.

[10] Frink, N., "Strategy for Dynamic CFD Simulations on SACCON Configuration," *28th AIAA Applied Aerodynamics Conference*, 2010, p. 4559.

[11] Hall, R., Biedron, R., Ball, D., Bogue, D., Chung, J., Green, B., Grismer, M., Brooks, G., and Chambers, J., "Computational Methods for Stability and Control (COMSAC): The Time Has Come," *AIAA Atmospheric Flight Mechanics Conference and Exhibit*, 2005, p. 6121.

[12] Lutz, T., Gansel, P. P., Waldmann, A., Zimmermann, D.-M., and Schulte am Hülse, S., "Prediction and Measurement of the Common Research Model Wake at Stall Conditions," *Journal of Aircraft*, Vol. 53, No. 2, 2016, pp. 501–514. https://doi.org/10.2514/1.C033351, URL http://arc.aiaa.org/doi/10.2514/1.C033351.

[13] Gansel, P. P., Illi, S. A., Krimmer, S., Lutz, T., and Krämer, E., "Unsteady CFD Simulation of the NASA Common Research Model in Low Speed Stall," *High Performance Computing in Science and Engineering '13*, Springer, 2013, pp. 439–453.

[14] Gansel, P. P., Illi, S., Lutz, T., and Krämer, E., "Numerical Simulation of Low Speed Stall and Analysis of Turbulent Wake Spectra," *15th International Conference on Fluid Flow Technologies, Budapest, Hungary*, 2012.

[15] Havas, J., and Rabadan, G., "Prediction of Horizontal Tail Plane Buffeting Loads," *International Forum on Aeroelasticity and Structural Dynamics Paper*, Vol. 128, 2009, p. 2009.

[16] Whitney, M. J., Seitz, T. J., and Blades, E. L., "Low-Speed-Stall Tail Buffet Loads Estimation Using Unsteady CFD," *International Forum on Aeroelasticity and Structural Dynamics (IFASD)*, 2009.

[17] Spalding, D. B., "A Novel Finite Difference Formulation for Differential Expressions Involving Both First and Second Derivatives," *International Journal for Numerical Methods in Engineering*, Vol. 4, No. 4, 1972, pp. 551–559.

[18] Lee, S. B., "A Study on Temporal Accuracy of OpenFOAM," *International Journal of Naval Architecture and Ocean Engineering*, Vol. 9, No. 4, 2017, pp. 429–438.

[19] Spalart, P. R., Deck, S., Shur, M. L., Squires, K. D., Strelets, M. K., and Travin, A., "A New Version of Detached-Eddy Simulation, Resistant to Ambiguous Grid Densities," *Theoretical and Computational Fluid Dynamics*, Vol. 20, No. 3, 2006, p. 181.

[20] The OpenFOAM Guide, "The PIMPLE Algorithm in OpenFOAM," Available at https://openfoamwiki.net/index.php/OpenFOAM_guide/The_PIMPLE_algorithm_in_OpenFOAM, 2018. Accessed: 2020-08-21.

[21] Lemaire, S., Vaz, G., and Turnock, S., "On The Need for Higher Order Interpolation With Overset Grid Methods," *22nd Numerical Towing Tank Symposium*, 2019.

[22] Jasak, H., and Tuković, Ž., "Dynamic Mesh Handling in OpenFOAM Applied to Fluid-Structure Interaction Simulations," *Proceedings of the V European Conference on Computational Fluid Dynamics ECCOMAS CFD 2010*, 2010.

[23] Shepard, D., "A Two-Dimensional Interpolation Function for Irregularly-Spaced Data," *Proceedings of the 1968 23rd ACM National Conference*, 1968, pp. 517–524.

[24] Wright, J., and Cooper, J., *Introduction to Unsteady Aerodynamics*, Vol. 20, John Wiley & Sons Ltd, Chichester, England, 2008.

[25] Cordes, U., Kampers, G., Meißner, T., Tropea, C., Peinke, J., and Hölling, M., "Note on the Limitations of the Theodorsen and Sears Functions," *Journal of Fluid Mechanics*, Vol. 811, 2017.

[26] Amiralaei, M., Alighanbari, H., and Hashemi, S., "An Investigation into the Effects of Unsteady Parameters on the Aerodynamics of a Low Reynolds Number Pitching Airfoil," *Journal of Fluids and Structures*, Vol. 26, No. 6, 2010, pp. 979–993.